

Article

LA-ICP-MS Analysis of Clinopyroxenes in Basaltic Pyroclastic Rocks from the Xisha Islands, Northwestern South China Sea

Yu Zhang ^{1,2,3}, Kefu Yu ^{1,2,3,*}  and Handong Qian ⁴

¹ Guangxi Laboratory on the Study of Coral Reefs in the South China Sea, Nanning 530004, China; haishuixing2@163.com

² Coral Reef Research Center of China, Guangxi University, Nanning 530004, China

³ School of Marine Sciences, Guangxi University, Nanning 530004, China

⁴ School of Earth Sciences and Engineering, Nanjing University, Nanjing, 2100093, China; qhd760@sohu.com

* Correspondence: kefuyu@scsio.ac.cn

Received: 5 October 2018; Accepted: 5 December 2018; Published: 7 December 2018



Abstract: Cenozoic volcanic rocks were recently discovered during full-coring kilometer-scale major scientific drilling in the Xisha Islands, northwestern South China Sea. A systematic mineralogical study of these samples was performed for this paper. The results show that the volcanic rock samples are basaltic pyroclastic. The major elements demonstrate that the clinopyroxenes are diopside and fassaite, which contain high Al₂O₃ (5.33–11.2 wt. %), TiO₂ (2.13–4.78 wt. %) and CaO (22.5–23.7 wt. %). Clinopyroxenes have high REE abundances (104–215 ppm) and are strongly enriched in LREE (LREE/HREE = 3.56–5.14, La/Yb_N = 2.61–5.1). Large-ion lithophile elements show depleted characteristics. Nb/Ta shows obvious fractionation features: Nb is lightly enriched, relative to primitive mantle, but Ta is heavily depleted, relative to primitive mantle. The parental magma of the basaltic pyroclastic rocks belongs to a silica-undersaturated alkaline series, characterized by a high temperature, low pressure, and low oxygen fugacity. The Al^{IV} content increases with decreasing Si concentration. The Si-unsaturated state causes Si-Al isomorphic replacement during the formation of clinopyroxene. The electric charge imbalance caused by the replacement of Si by Al is mainly compensated by Fe³⁺. The clinopyroxene discrimination diagrams show that the parental magma formed in an intraplate tectonic setting environment.

Keywords: clinopyroxene; LA-ICP-MS; mineral chemistry; Cenozoic; South China Sea

1. Introduction

As one of the largest marginal seas of Eastern Asia, the South China Sea (SCS) is located at the intersection of the Eurasian Plate, the Pacific Plate, and the Indian Ocean-Australian Plate. In the SCS and its adjacent areas, Cenozoic magmatism is relatively active, and Cenozoic igneous rocks are widely distributed. The Cenozoic igneous rocks are mainly characterized by basaltic rocks, volcanic clastic rocks, and intermediate-acid extrusive rocks [1–6]. For a long time, domestic and foreign scholars performed a lot of research on the Cenozoic basalts of the SCS. However, research on single minerals in the Cenozoic basalts of the SCS is still limited. As a petroprobe for most geological processes, igneous activity plays an important role in the study of petrology and tectonics. However, previous studies mainly focus on the petrology and geochemistry of the Cenozoic basalts [3,7–15]. There are few studies on the rock-forming minerals of basalt from the SCS and its adjacent areas [2,16,17], which seriously restricts research on the magma evolution and physicochemical conditions of Cenozoic basic rocks in the SCS and its adjacent areas.

The mineral composition of igneous rocks depends on the chemical composition and crystallization environment of magma. Changes in mineral composition and structure are direct evidence of changes in the diagenetic environment and material composition. Therefore, the characteristics of mineral composition can be used to explore mineral petrogenesis and the magma evolution mechanism [18]. Clinopyroxene is one of the main rock-forming minerals of mafic-ultramafic rocks and plays a major role in the generation and subsequent differentiation of magma [16,19–24]. Clinopyroxene composition mainly depends on primary magma characteristics, the crystallization environment, and the tectonic setting of magmatism [25–32]. Relative to other minerals in mafic-ultramafic rocks, clinopyroxene is considered to be the main carrier for most trace elements and holds a unique further record of magma history [33,34]. The mineral chemistry of relict clinopyroxene in igneous rocks can reflect the characteristics of the primary magma well and has been widely used to study the nature of the original magma and complicated processes that have affected the lithospheric mantle [21,35–42]. Furthermore, clinopyroxenes in altered basalts are of interest, because they often survive in a relatively pristine form, after the matrix and other minerals have been converted to secondary minerals. The major- and minor-element geochemistry of clinopyroxene is varied and provides a filtered view of the composition of the magma from which the clinopyroxene crystallized, lending it the potential to provide insight into the tectonic origins of altered basalts [43].

The general chemical formula of pyroxene can be expressed as $X(M_2)Y(M_1)[T_2O_6]$, where M_2 refers to cations with a generally distorted octahedral coordination ($X = Ca^{2+}, Na^+, Mg^{2+}, Fe^{2+}, Mn^{2+}$ and Li^+), M_1 refers to cations with a regular octahedral coordination ($Y = Mg^{2+}, Fe^{2+}, Mn^{2+}, Al^{3+}, Fe^{3+}, Cr^{3+}$ and Ti^{4+}), and T refers to a tetrahedrally coordinated cation (Si^{4+}, Al^{4+} , and minor Fe^{3+}) [44]. The analysis of the isomorphic replacement process is of great significance for further understanding the chemical compositions and genesis of pyroxene [23,45,46].

Volcanic rocks could be used as a probe for deep processes and magmatic activities. However, due to the thick sediments on the seafloor in the SCS, it is difficult to extract the volcanic rocks from the SCS. In this study, the mineral chemistry of newly obtained basaltic pyroclastic rock samples from Well CK-2 was analyzed to explore the origin of the clinopyroxene and primary magma. It is of great significance for understanding the characteristics of the Cenozoic basalts in the SCS and the formation and evolution of basaltic magma. The results will provide new evidence for the comprehensive understanding of the characteristics of Cenozoic magmatism in the SCS and the northern margin.

2. Geological Setting and Sample Description

The SCS is one of the largest marginal basins in the Western Pacific Ocean, which is bordered by the South China Block, Indochina Block, Luzon arc and Palawan. The SCS developed from Cenozoic continental margin rifting, and its central portion has a floor of oceanic crust. The SCS can be divided into three parts: the northern continental margin, the ocean basin, and the southern continental margin. Tectonically, the northern margin belongs to an extensional region, which is located between the South China Block and the SCS continent-ocean transition zone. The western margin is a strike-slip and pull-apart zone. The eastern and southern margins are mainly a compressive subduction zone, including the Manila Trench and the Nansha Trough. There are several small micro-continental blocks dispersed in the SCS, such as the Zhongsha block, the Xisha block, the Dongsha block, the Nansha block, and Reed-Northeastern Palawan block [7,47,48]. In addition, these micro-continents may have previously existed as a whole in a large micro-block. These blocks began to separate from each other due to rifting and spreading of the SCS. The times of the beginning and end of SCS expansion have been investigated for many years based on geophysical data in the central ocean basin [49–51]. With the continuous advancement of the International Ocean Discovery Program (IODP), Li et al. [52,53] determined that the expansion of the SCS started at 33 Ma and stopped at approximately 15 Ma, based on the investigations of the IODP 349 expedition.

Cenozoic igneous rocks are widely distributed in the SCS and its surrounding areas. According to the relationship with SCS spreading events, Cenozoic volcanism in the SCS and its surrounding

areas are divided into three groups: pre-spreading, syn-spreading, and post-spreading [4,5,54]. The pre-spreading volcanism is mainly distributed along the northern margin of the SCS and the coastal areas of South China. The syn-spreading volcanism is relatively weak, and a limited to basaltic volcanism is found in the Pearl River Mouth Basin. After the SCS stopped expanding, large-scale intraplate magmatism occurred in the SCS and its surrounding areas, e.g., Leizhou Peninsula, Hainan Island, Vietnam and the SCS basin [4,9,55].

The clinopyroxene studied in this paper is from the basement rocks of Well CK-2, which is located on Chenhang Island, Xisha Islands (also known as the Paracel Islands [56]) (Figure 1) ($110^{\circ}0'53.557''\text{E}$, $16^{\circ}26'56.368''\text{N}$). This well is a major scientific research drilling project. The basement of Well CK-2 consists of basaltic pyroclastic rocks. The basaltic pyroclastic rocks have conformable contacts with underlying carbonate rocks. Zircon U-Pb ages suggest that the basaltic pyroclastic rocks were deposited as early as 35.5 ± 0.9 Ma [57]. The volcanic clastic rocks contain a small number of marine bioclastic fossils, sometimes with reef limestone breccia. The colors of the basaltic volcanic clastic rocks are grey green, dark green and yellowish-brown. The basaltic rocks from Well CK-2 are extensively altered (chloritization, serpentinization and carbonation). The phenocryst minerals mainly consist of clinopyroxene. The main mineral components of the matrix are slender strip plagioclase, granulated pyroxene, and basalt glass. Clinopyroxene occurs as euhedral, subhedral or skeletal crystals, and lacks reaction and rimming relationship. The pores are linked with each other in a series. The amygdules are mainly round and elliptical, with a small number of irregular ones in some parts, and the filling minerals are mainly calcite, zeolite, opal, and chalcedony (Figure 2). The rocks have developed igneous textures and structures, such as aphanitic textures, vesicular structures, and amygdaloidal structures. Sample 170 h is from the middle part of the basaltic pyroclastic rocks (908 m), and zr1h is from the upper part of the basaltic pyroclastic rocks (885 m). The clinopyroxenes that are used for analysis do not have a zoned texture.

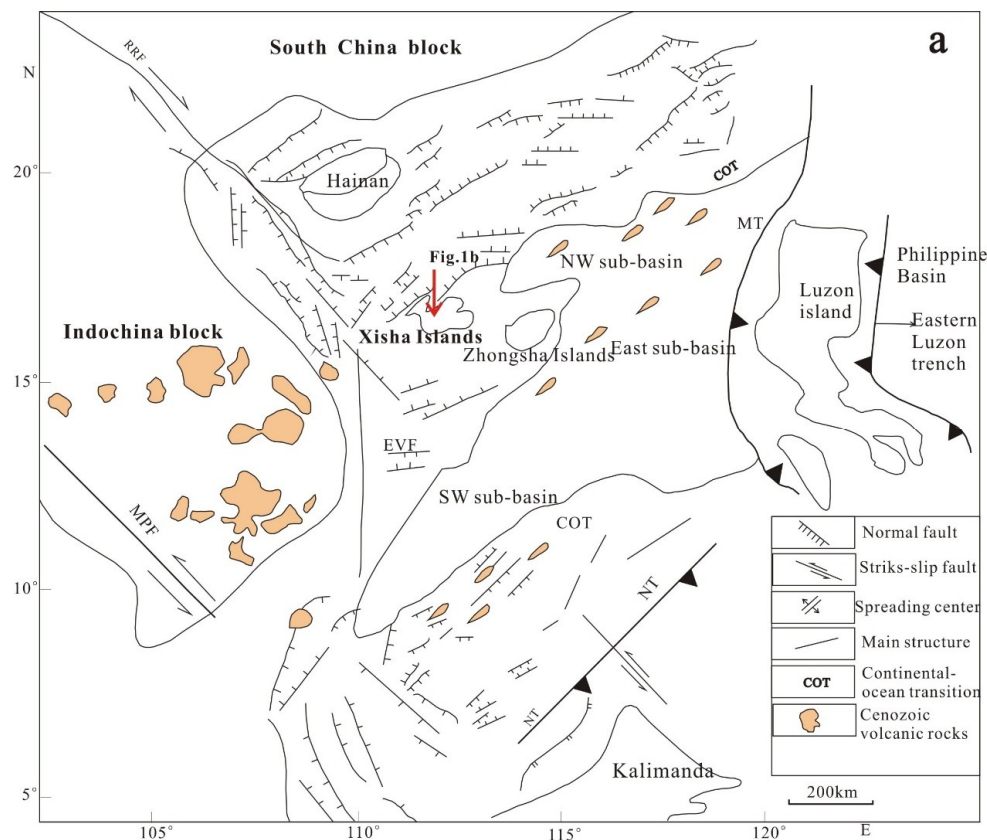


Figure 1. Cont.

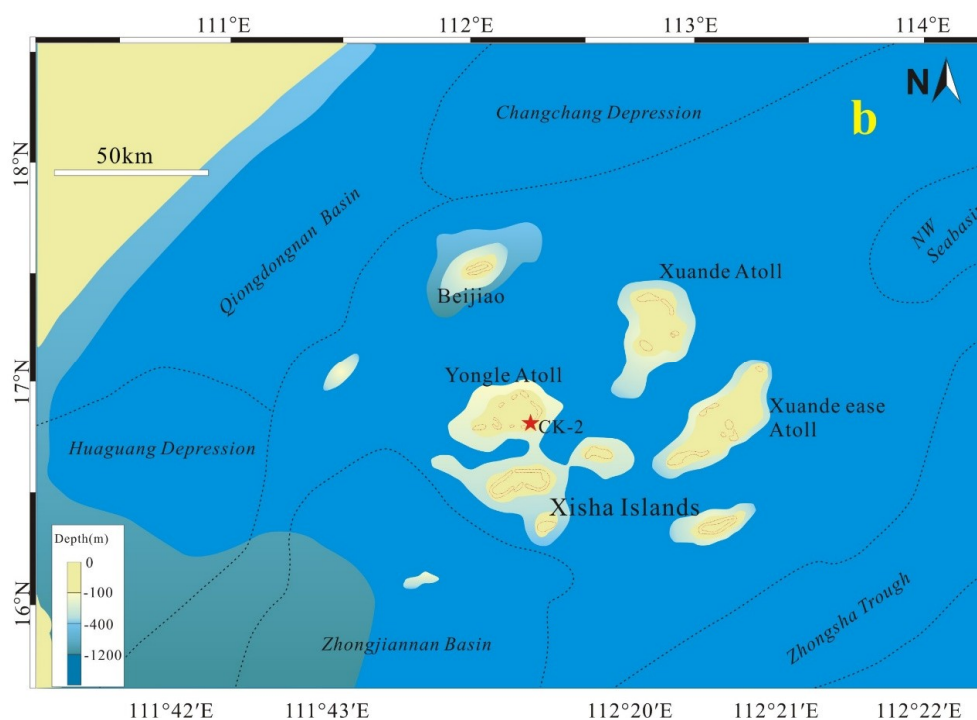


Figure 1. (a) Geological sketch of the South China Sea and its adjacent areas; (b) location of Well CK-2 (after polarization [7,56]). The depth is below sea level and in meters.



Figure 2. Photographs of the basaltic pyroclastic rocks under the microscope (cross polarized). Labels represent: Px-pyroxene; Pl: plagioclase. (a) pyroxene phenocryst in basaltic pyroclastic rocks; (b) amygdala in basaltic pyroclastic rocks

3. Analytical Methods

Major and trace element analyses of clinopyroxene were conducted with an Agilent 7500× ICP-MS, equipped with a GeoLas Pro 193 nm ArF excimer laser-ablation system, installed in the State Key Laboratory of Ore Deposit Geochemistry, Institute of Geochemistry, Chinese Academy of Sciences (Guiyang, China). Helium was applied as a carrier gas, which was mixed with argon via a T-connector before entering the ICP-MS. Each analysis incorporated a background acquisition of approximately 30 s (gas blank), followed by 50 s of data acquisition from the sample. Element contents were calibrated against multiple-reference materials (NIST 610, BCR-2G, BIR-1G and BHVO-2G), without applying internal standardization [58]. The preferred values of element concentrations for the reference

glasses are from the GeoReM database [59]. Off-line selection and integration of background and analyte signals, time-drift correction and quantitative calibration were performed by ICPMSDataCal 10.8 [58,60]. Representative results of each of the analyzed phases and standard reference material are provided in Tables S1 and S2. The analysis of most of the elements has an accuracy of less than 5% and a precision greater than 10%.

4. Mineral Composition of Clinopyroxenes

4.1. Major Element Composition of Clinopyroxenes

The major element compositions of the clinopyroxenes are listed in Table S3. The data were processed with the geochemical software tool “Geokit” [61]. LA-ICP-MS analyses show that clinopyroxenes have a variable compositional range, with Al_2O_3 (5.33–11.18 wt. %), FeO (6.05–8.22 wt. %), MgO (10.79–14.46%), CaO (22.5–23.73 wt. %), MnO (0.12–0.15 wt. %), and TiO_2 (2.13–4.78 wt. %) contents. The chemical composition of monoclinic pyroxene varies widely, indicating that it has experienced a relatively strong degree of crystallization differentiation. The $\text{Fe}^{2+}/(\text{Fe}^{2+} + \text{Fe}^{3+})$ values of clinopyroxenes are relatively high, ranging from 0.64 to 0.96 (with an average value of 0.8), implying that the oxygen fugacity was relatively low [62]. The $\text{Ca}/(\text{Ca} + \text{Mg} + \text{Fe})$ values range from 0.47 to 0.52 ($\text{Fe} = \text{Mn} + \text{Fe}^{2+} + \text{Fe}^{3+}$), with an average of 0.49, indicating that clinopyroxene has a high Ca content. Overall, the chemical compositions of the clinopyroxenes change widely, and the clinopyroxenes are characterized by high Ca, Al and Ti.

All clinopyroxenes from Well CK-2 are located in the field of the Ca-Mg-Fe pyroxene group in the Q-J diagram proposed by Morimoto et al. [63] (Figure 3a). In the conventional Wo-En-Fs diagram [63], most of the clinopyroxene plots in the diopside field, and a few clinopyroxenes fall into the fassaite field (Figure 3b). In the main cation correlation diagram (Figure 4), Al ($\text{Al}^{\text{IV}} + \text{Al}^{\text{VI}}$) and Ti have strong negative correlations with Mg ($r = -0.98$ and -0.97 , respectively), and Si has a strong positive correlation with Mg ($r = 0.95$).

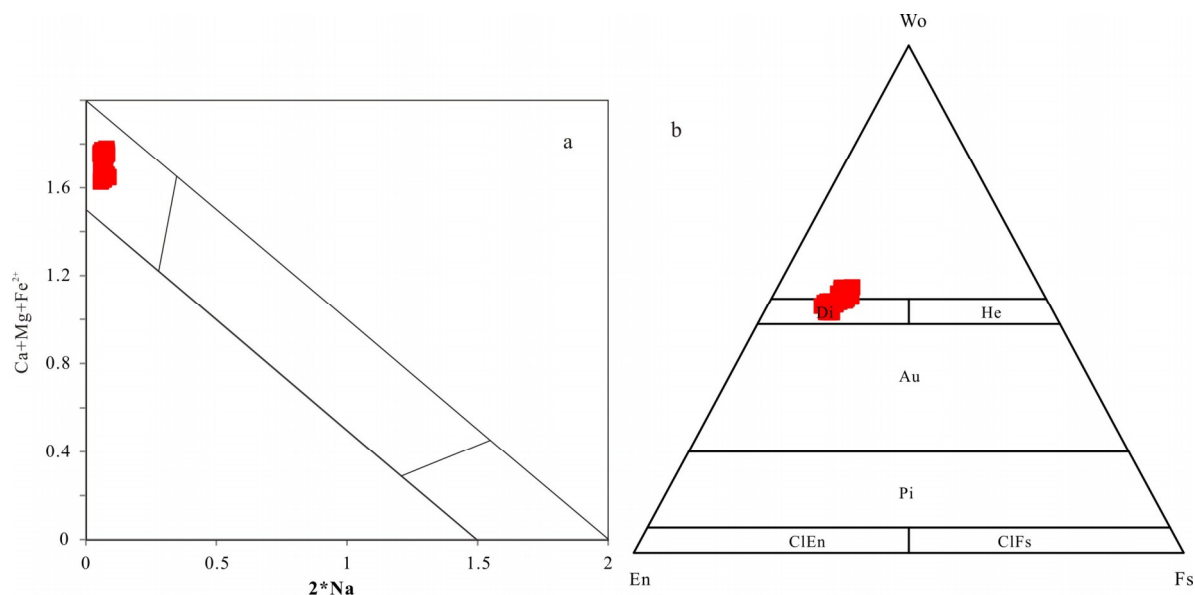


Figure 3. (a) Plot of a series discrimination diagram for clinopyroxenes; (b) Wo-En-Fs classification diagram for clinopyroxenes (after Morimoto [63]). Di-diopside, He-hedenbergite, Au-Augite, Pi-Pigeonite, ClEn-clinoenstatite, ClFs-clinoferrosilite.

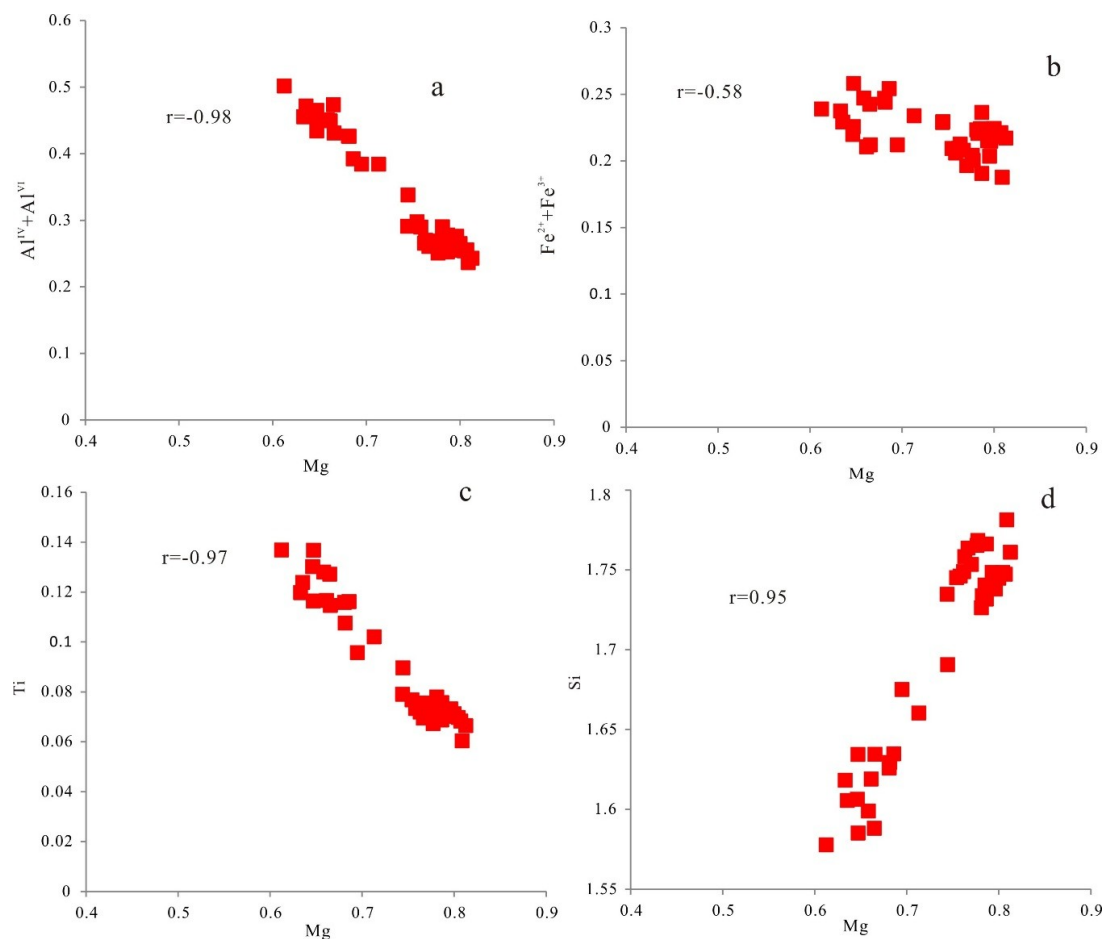


Figure 4. Plots of Mg contents vs. concentrations of other cations in clinopyroxenes. (a) $Al^{IV} + Al^{VI}$ vs. Mg; (b) $Fe^{2+} + Fe^{3+}$ vs. Mg; (c) Ti vs. Mg; (d) Si vs. Mg

4.2. Trace Element Composition of Clinopyroxenes

The trace element and REE compositions of clinopyroxenes from the basaltic pyroclastic rocks are shown in Table S4. The Σ REE of these clinopyroxenes is relatively high and varies from 104 ppm to 215 ppm, with an average of 145 ppm, which is higher than the results from previous studies (with an average value of 62 ppm) [2]. The chondrite-normalized REE patterns show LREE enrichment, with high ratios of LREE/HREE (Figure 5) (3.56–5.14, with an average value of 4.22) and $(La/Yb)_N$ (2.61–5.1, with an average value of 3.79). This inverted U-shaped REE distribution pattern may be related to fluid replacement [64]. There are no obvious Eu anomalies in the REE distribution patterns ($\delta Eu = 0.85$ – 0.98 , with an average value of 0.92). The enrichment and depletion of Eu mainly depend on the aggregation and migration of calcium-bearing rock-forming minerals, which are constrained by the conditions of rock formation. The weakly negative Eu anomalies indicate that plagioclase fractionation is slight during the formation and evolution of the magma, which is consistent with the petrographic observation that plagioclase phenocrysts are scarce in the rocks.

In the primitive mantle-normalized trace element spider diagrams (Figure 6), most of the samples show similar distribution patterns. One sample (170 h-15) has anomalously high Pb. As Pb exists mainly in the form of isomorphism, we suggest that this may reflect the degree of isomorphism. However, further research is required to determine this. Large-ion lithophile elements (LILE) (such as Sr and Ba) show depleted characteristics. Sr and Ba do not easily form independent minerals in magmatic rocks. These elements are mainly available in K-rich, Ca-rich minerals in the form of isomorphism. The depletion of Sr and Ba may be caused by a small amount of plagioclase, crystallized in the early stage or by magma derived from depleted mantle [65]. In addition, in the primitive mantle,

normalized trace element pattern Nb/Ta fractionation is obvious. Nb shows negative anomalies, and Ta has significant positive anomalies, which is consistent with their distribution coefficients between clinopyroxene and melt, indicating that the main cause of their fractionation is the crystallization differentiation of clinopyroxene.

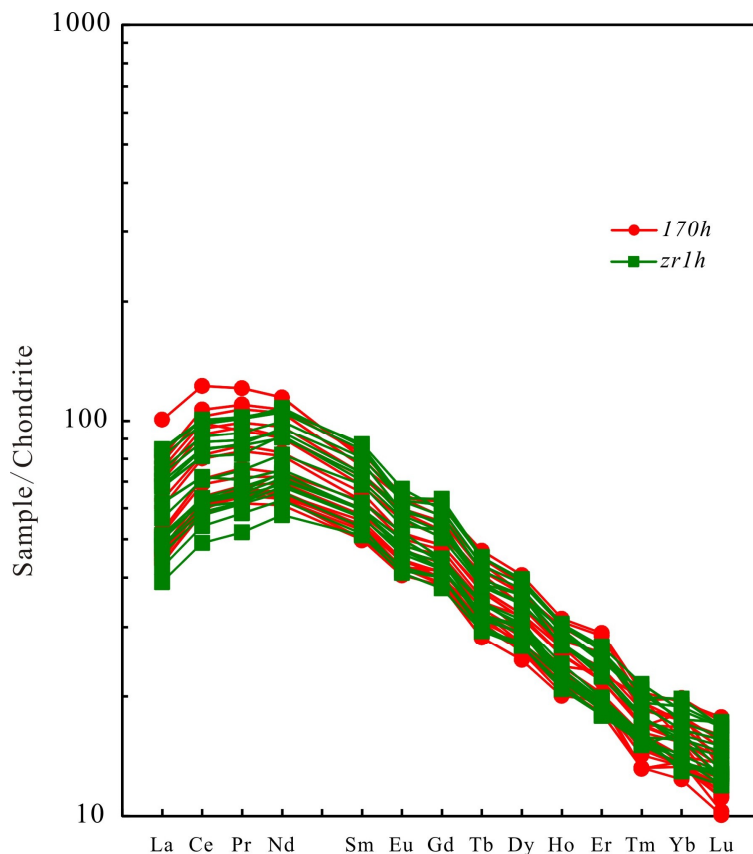


Figure 5. Chondrite-normalized REE abundance patterns for the clinopyroxenes from Well CK-2.

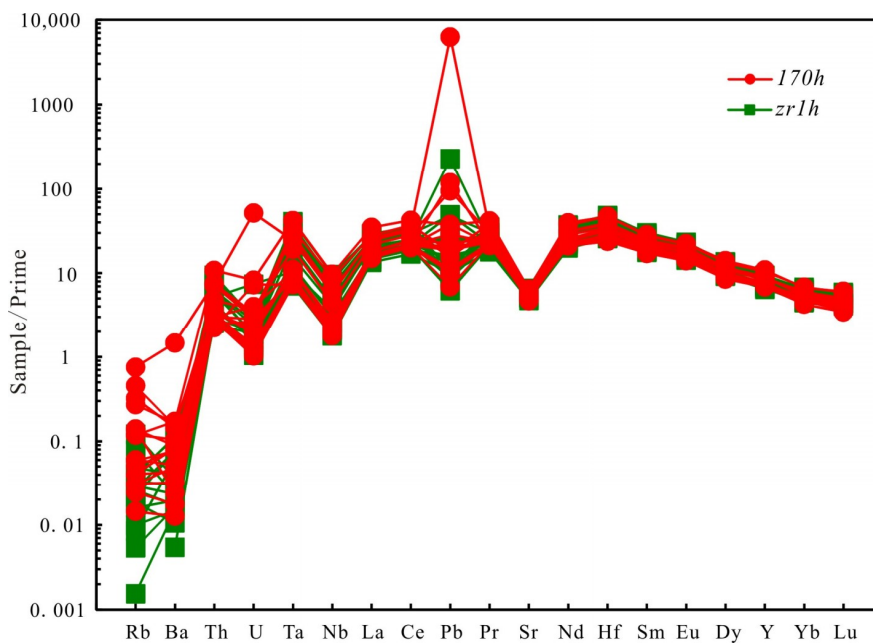


Figure 6. Multiple trace element patterns, normalized to the primitive mantle for the clinopyroxenes from Well CK-2.

5. Discussion

5.1. The Relationship between Clinopyroxene and the Host Rock

According to the chemical composition and structural characteristics of clinopyroxene, Wass [62] classifies clinopyroxene into four types. (1) Cr-diopside represents the accidental capture of mantle minerals. Cr-diopside always has textures consistent with a metamorphic origin and has relatively high SiO_2 and Cr_2O_3 , low TiO_2 and moderate Al_2O_3 . (2) Al-augite results from accidentally included xenoliths of a basaltic composition, which are crystallized from a previous melting event in the mantle and crust-mantle transition zone. These Al-augites have a variety of structures, such as modified igneous textures, recrystallization, and metamorphic structures, due to varying degrees of subsolidus grain-boundary adjustment. (3) Al-augite, as discrete megacrysts or in xenoliths, which is crystallized from a primitive alkaline basaltic magma under high pressure, is associated with the host rock. Grey-white reaction edges are generally developed around round or angular pyroxene fragments. (4) The fourth type of clinopyroxene, crystallized from basaltic magma at low pressure, is easily distinguished from the other three types. This type forms small, euhedral crystals and lacks reaction and rimming relationships. The most significant feature of this type is the high proportion of Al, which is accommodated in the tetrahedral site, reflected by the ratio of $\text{Al}^{\text{IV}}/\text{Al}^{\text{VI}}$. The clinopyroxenes from Well CK-2 have high ratios of $\text{Al}^{\text{IV}}/\text{Al}^{\text{VI}}$, ranging from 5 to 105. Furthermore, combining this information with mineralogical structural features, we suggest that the clinopyroxenes from Well CK-2 belong to the fourth type and are crystallized from basaltic magma at low pressure.

5.2. The Nature of Parental Magma

It is demonstrated that the Al_2O_3 content of clinopyroxenes crystallized from a magma is mainly controlled by the SiO_2 content of the magma [25,26,66,67]. Clinopyroxenes from oversaturated tholeiitic magmas have high Si/Al ratios, while those from undersaturated alkali basalt have low Si/Al ratios [25,62,68]. The content of Al_2O_3 in diopside is generally 1–3 wt. % [69]. The clinopyroxenes from Well CK-2 have relatively high Al_2O_3 (5.33–11.18 wt. %) and low SiO_2 contents (41.44–47.02 wt. %), implying that these clinopyroxenes are formed from undersaturated alkaline basaltic magma. Gibb [70] pointed out that clinopyroxenes tend to be more Ca-rich when the magma is more silica-undersaturated. The clinopyroxenes from Well CK-2 present the characteristic of a high Ca content, with $\text{Ca}/(\text{Ca} + \text{Mg} + \text{Fe})$ ratios of 0.47–0.52, implying that the clinopyroxenes were crystallized from a low-Si magma [70].

In pyroxene, the coordination of Al is closely related to temperature and pressure and has important typomorphic significance [63]. High temperature and low pressure favor a low coordination of aluminum (Al^{IV}). In contrast, low temperature and high pressure favor a high coordination of aluminum (Al^{VI}) [71]. The Al^{IV} of the clinopyroxene from these basaltic rocks varies from 0.22 to 0.42, with an average of 0.3. The $\text{Al}^{\text{IV}}/\text{Al}^{\text{VI}}$ ratio of clinopyroxenes increases with decreasing pressure values in a variety of petrological environments [62,72,73]. The $\text{Al}^{\text{IV}}/\text{Al}^{\text{VI}}$ ratios of the clinopyroxenes in this study are relatively high and vary from 5.1 to 105.71, with an average of 19.36 [71,74–78]. The high $\text{Al}^{\text{IV}}/\text{Al}^{\text{VI}}$ ratios (5.1–105.71) of clinopyroxenes from Well CK-2 suggest relatively low-pressure environments for crystallization [62]. Thompson [73] suggested that the Al^{VI} content increases with increasing pressure. The clinopyroxenes from Well CK-2 have only 0.0024–0.0795 cations Al^{VI} . As compared to the experimental data of Thompson [73], this suggests pressures below 10 kbar. In the $\text{Al}^{\text{VI}}\text{-Al}^{\text{IV}}$ discrimination diagram (Figure 7a), all sample plots in the low-pressure field [71].

Based on research on the distribution of Ti in the silicates and oxides of magmatic rocks, Verhoogen [26] proposed that the crystallization temperature of clinopyroxene was positively correlated with its Ti content. Thus, the higher the crystallization temperature of the clinopyroxene, the more Ti clinopyroxene is likely to contain [26]. The TiO_2 content of clinopyroxenes from the Well CK-2 is higher (2.13–4.78 wt. %) than that of clinopyroxenes from the Cenozoic basalt in the

SCS (0.85–2.23 wt. %) [16], implying that the clinopyroxenes from Well CK-2 have a relatively high crystallization temperature, compared to the clinopyroxenes from the Cenozoic basalt in the SCS. In the $\text{SiO}_2\text{-Al}_2\text{O}_3$ discrimination diagram of clinopyroxenes (Figure 7b), all data plots in the field of the peralkaline-alkaline region. Meanwhile, in the Ti-(Ca + Na) diagram (Figure 7c), all the samples lie within the field of alkali basalt, as illustrated by Leterrier et al. [28]. Both discrimination diagrams show a relatively consistent conclusion: the parental magma of the basaltic rocks in the study should have been alkaline magma. As mentioned above, the clinopyroxenes show high Al and Ti contents, which is consistent with the evolution trend of an alkaline magma.

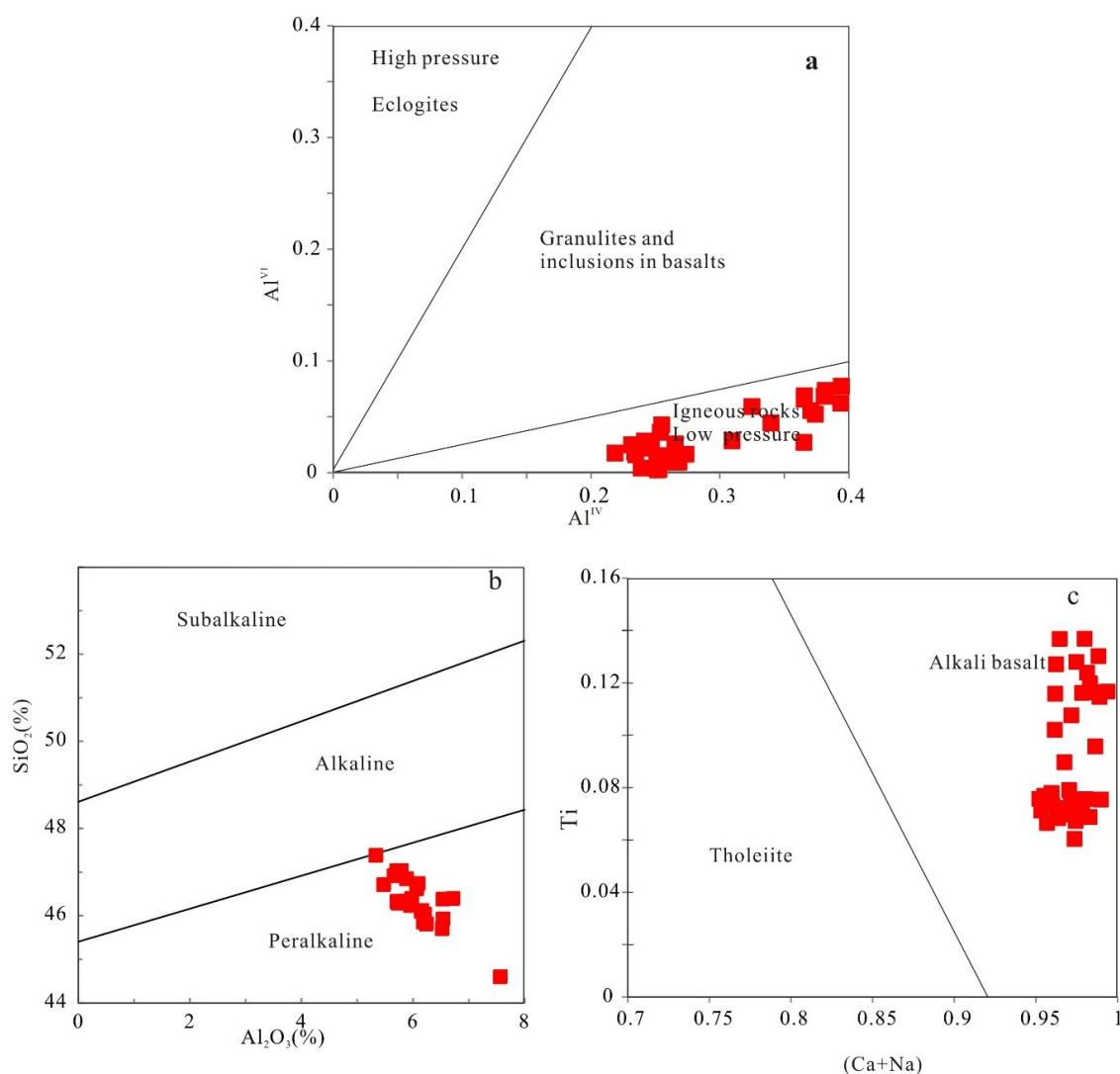


Figure 7. (a) Compositions of clinopyroxenes in the Al^{VI} (apfu) versus Al^{IV} (apfu) discrimination diagrams (after Aoki and Shiba, [68]). (b) $\text{SiO}_2\text{-Al}_2\text{O}_3$ discrimination diagrams for clinopyroxenes (after Leterrier et al. [28]); (c) Plot of clinopyroxenes on the (Ca + Na)-Ti discrimination diagram (after Leterrier et al. [28]).

Classic studies on the clinopyroxene in basic igneous rocks show that pyroxene crystallizing in basalt magma usually has monoclinic enstatite and clinopyroxene, and the Ca content of the clinopyroxene is very low [68]. However, there is only clinopyroxene in alkaline magma, and enstatite is rarely found. The content of Ca in clinopyroxene is relatively high. The high Ca content of clinopyroxene from Well CK-2 implies that the parental magma may have been an alkaline magma. Furthermore, Qiu and Liao [43] suggest that the clinopyroxene from alkaline series rocks has a high

value of Wo and evolves in the direction of En-poor and Wo-rich. Titanaugite is a mineral symbolic of alkaline series basalt. The contents of TiO₂ and Wo in clinopyroxene from Well CK-2 are relatively high, and the content of En is relatively low, indicating that the parental magma was an alkaline magma, which is consistent with the alkaline discrimination diagram of clinopyroxene.

Trace element abundances in clinopyroxene reflect the trace element contents of the parental magma when the mineral grains segregate, which provides some clue as to the chemical composition of the parental magma [35,67]. REE exist mainly in the form of isomorphism in pyroxene. The clinopyroxenes from Well CK-2 belong to Ca-Mg-Fe series, which are beneficial to the isomorphism of REE [69]. Isomorphic replacement among cations in pyroxenes is a very common but complicated phenomenon. The change in elemental content reflects the difference in the degree of isomorphism, which may be due to the fractional crystallization. The clinopyroxene chondrite-normalized REE patterns and primitive mantle-normalized trace element patterns of the clinopyroxenites from Well CK-2 all show a similar LREE enrichment, depletion in Sr, Ba and Ta, and enrichment in Nb, suggesting that these clinopyroxenes are all derived from magma, with the same trace element characteristics. To further study the chemical composition of the parental magma, we calculated the REE contents of the hypothetical parental melt in clinopyroxene using the clinopyroxene/melt partition coefficient (Table S5) [34,64]. In the calculated chondrite-normalized REE diagram (Figure 8), all data for the calculated melts show a very strong enrichment in LREE. The calculated melt REE distribution patterns are similar to those of the volcanic rocks from the SCS and its surrounding areas [3,4,7–10,15,17,36,55,79,80] and to the typical intraplate oceanic island basalts (OIB) [81].

In general, the mineralogical characteristics of the clinopyroxene from Well CK-2 reveal that the parental magma should have belonged to an alkaline series, characterized by a high temperature, low pressure, low Si content, high Ca content and low oxygen fugacity.

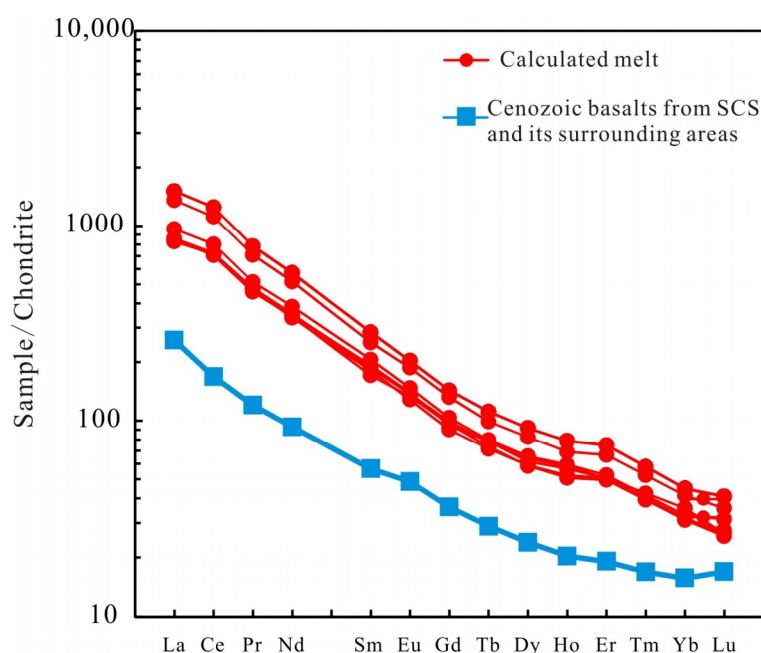


Figure 8. Calculated chondrite-normalized REE patterns of the parental magma of the clinopyroxenes. The hypothetical melt is compared to the intraplate basalt. Data for the Cenozoic basalts are from [7].

5.3. Isomorphic Replacements in Clinopyroxenes

In Figure 9a, Al^{IV} is shown to have a strong linear relationship with Si. The linear equation is $y = 2 - x$ (where x and y represent Si and Al^{IV}, respectively), implying that the insufficiency caused by the shortage of Si in the tetrahedral position is mainly supplemented by Al^{IV} [63]. At the same time, some of the Al^{VI} substitutes for ^{M1}Mg in the octahedral sites maintain the electrovalence balance,

forming $\text{CaMgAl}^{\text{VI}}\text{Al}^{\text{IV}}\text{SiO}_6$ ($^{\text{M1}}\text{Mg} + ^{\text{T}}\text{Si} = \text{Al}^{\text{IV}} + \text{Al}^{\text{VI}}$). The Al^{VI} , which occupies the position of M1, accounts for 0 to 16% of all Al, with an average of 9%.

In addition to Al^{IV} , the octahedral position still requires additional cations to compensate for the electric charge imbalance caused by the replacement of Si by Al^{IV} , such as Fe^{3+} and Ti^{4+} . However, previous studies have shown that Fe^{3+} preferentially entered octahedral sites rather than Ti, and only a small amount of Ti in the octahedra is used to compensate for the excess negative charge caused by the replacement of Si by Al^{IV} [19,63]. The corresponding alternative reaction formula for the replacement of Mg by Ti is: $^{\text{M1}}\text{Mg} + ^{\text{T}}2\text{Si} = ^{\text{M1}}\text{Ti} + ^{\text{T}}2\text{Al}^3$. The (Mg + 2Si) has a good correlation with (Ti + $^{\text{T}}2\text{Al}$) ($r = -0.996$) (Figure 9b), although most of the Ti is independent of the equilibrium charge and enters the octahedral sites to form titaugite ($\text{NaMg}_{0.5}\text{Ti}_{0.5}\text{Si}_2\text{O}_6$) by the alternative equation $\text{Ca} + \text{Mg} = \text{Na} + \text{Mg}_{0.5}\text{Ti}_{0.5}$ [19,63]. Thus, we conclude that the electric charge imbalance caused by the replacement of Si by Al is mainly compensated by Fe^{3+} . The corresponding alternative reaction formula is: $^{\text{M1}}\text{Mg} + ^{\text{T}}\text{Si} = ^{\text{M1}}\text{Fe}^{3+} + ^{\text{T}}\text{Al}^{\text{IV}}$, forming calcium iron aluminum pyroxene (CaFeAlSiO_6). In Figure 9c, (Mg + Si) and ($\text{Fe}^{3+} + \text{Al}$) are shown to have a good negative linear relationship ($r = -0.90$), implying that the octahedral bound, Fe^{3+} , entered the pyroxene crystal structure and replaced Mg^{2+} to compensate for the electric charge imbalance caused by the replacement of Al^{IV} by Si. Furthermore, in Figure 9d, Na is shown to have a significant negative correlation with Si ($r = -0.92$), suggesting that Na and Fe^{3+} participate in the replacement reaction during the late stage of the formation of clinopyroxene ($\text{Ca} + \text{Mg} = \text{Na} + \text{Fe}^{3+}$). The contents of Ti and Fe^{3+} control the content of Na in clinopyroxene.

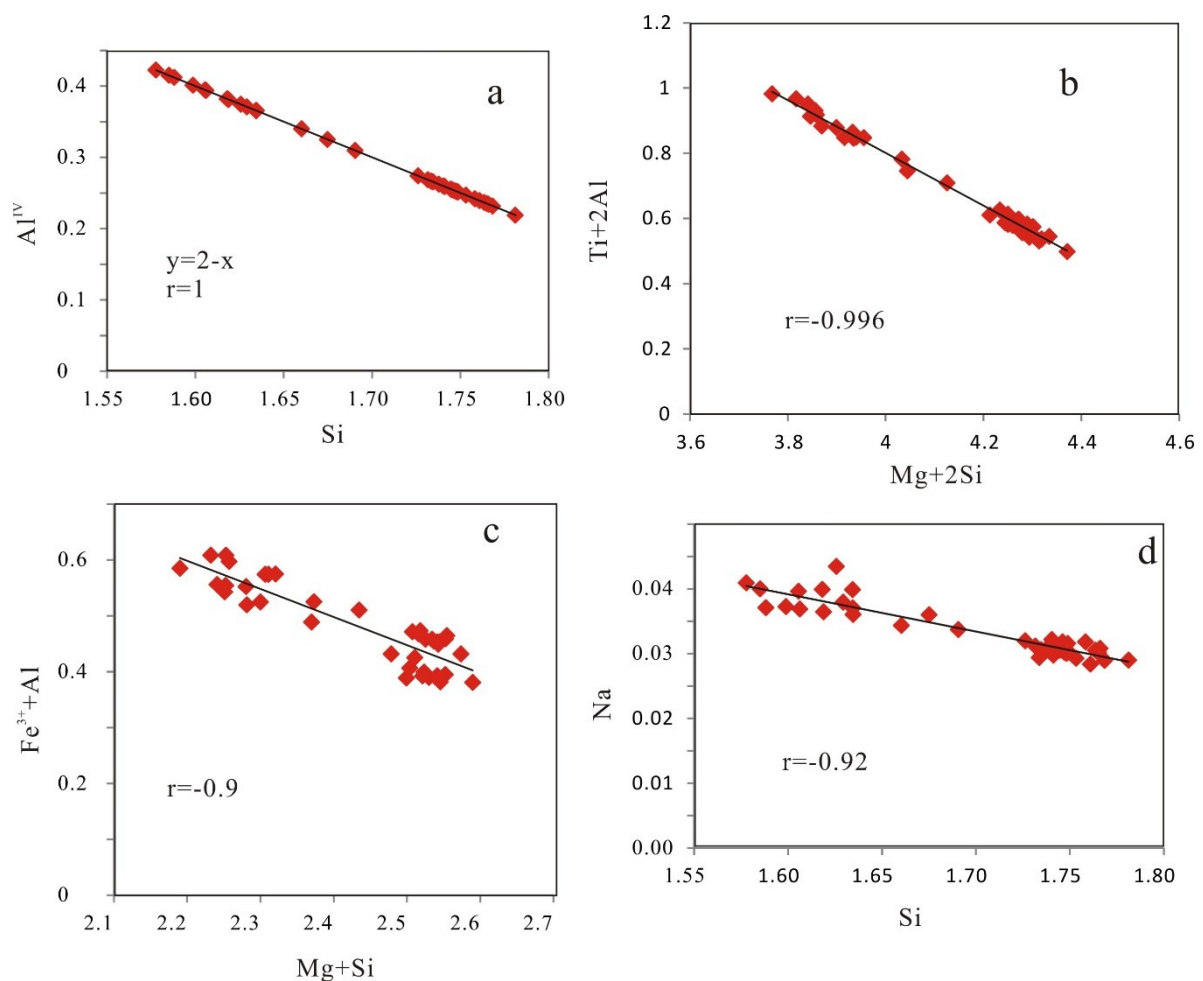


Figure 9. Element isomorphous replacements in the clinopyroxenes from Well CK-2 (based on 6 oxygen atoms). (a) Al^{IV} vs. Si; (b) $\text{Ti}+2\text{Al}$ vs. $\text{Mg}+2\text{Si}$; (c) Fe^{2+} vs. $\text{Mg}+\text{Si}$; d: Na vs. Si.

The Al^{IV} content in clinopyroxene mainly depends on the content of SiO_2 in magma. The Al^{IV} content increases with decreasing Si concentration [26]. The basaltic pyroclastic rocks belong to the Si-unsaturated alkaline rock series. The Si-unsaturated state causes the Si-Al replacement during the formation of clinopyroxene. The low oxygen fugacity implies that the main role of Fe^{3+} is to balance the electric charge. The majority of the Ti enters the octahedral sites to form titanite. The electric charge imbalance caused by the replacement of Si by Al is mainly compensated by octahedral Fe^{3+} . No aegitite was observed in the samples.

5.4. Tectonic Setting Discrimination

Nisbet and Pearce [27] constructed two discrimination diagrams using the main oxide mass fraction of clinopyroxene to determine the tectonic setting of the host rock: the F1-F2 diagram of clinopyroxenes, and the TiO_2 - Na_2O - MnO triangular diagram. The two discrimination diagrams can distinguish basaltic clinopyroxenes from volcanic arc basalt (VAB), ocean floor basalt (OFB), within-plate tholeiite (WPT), and within-plate alkalic (WPA) environments. Both discrimination diagrams are successful in distinguishing the within-plate alkali basalts, because their pyroxenes characteristically have low Si and high Ti and Na contents [27]. In the F1-F2 tectonic environment discrimination diagram (Figure 10) [27], all the samples in this study fall into the field of WPA basalts. In addition, in the TiO_2 - Na_2O - MnO triangular discrimination diagram (Figure 10) [27], all the clinopyroxenes are distinctly concentrated in the field of WPA, suggesting that these basaltic pyroclastic rocks are likely to be within-plate basalts. This interpretation is also supported by plotting the pyroxene analyses in the diagrams of Leterrier et al. [28] (Figure 7c).

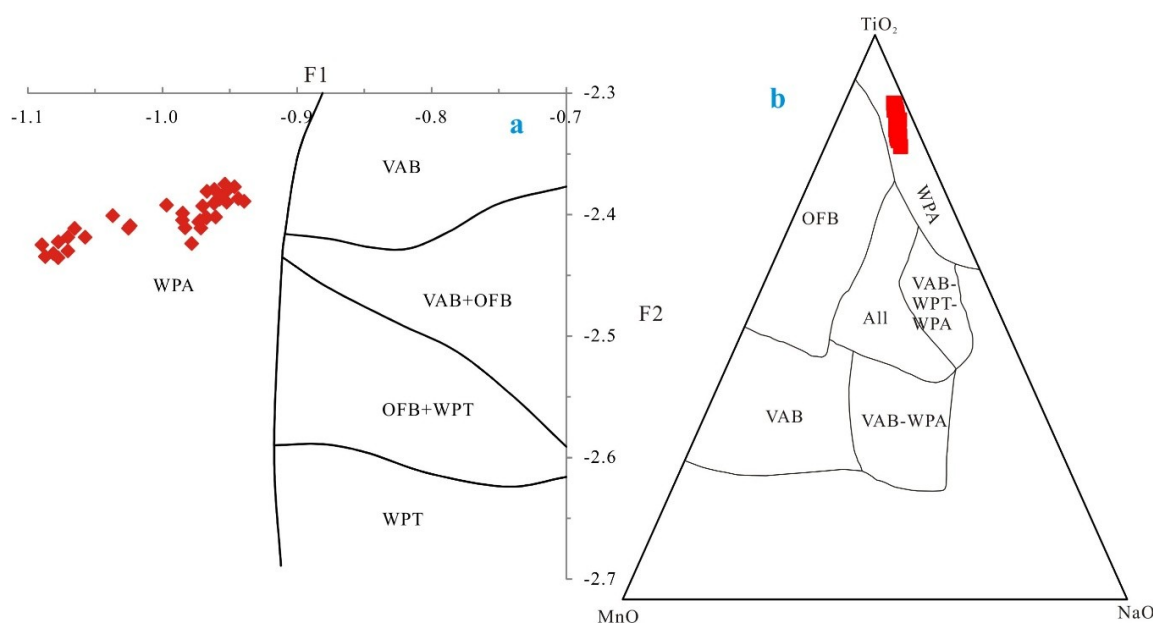


Figure 10. Tectonic discrimination diagram, proposed by Nisbet and Pearce [27]. (a) F1 vs. F2 tectonic discrimination diagrams; (b) TiO_2 - MnO - Na_2O tectonic discrimination diagram. WPT: within-plate tholeiitic basalt; WPA: within-plate alkali basalt; VAB: volcanic arc basalt; and OFB: ocean floor basalt.

Another attempt to distinguish basalt compositions based on clinopyroxene compositions was presented by Aparicio [30]. Based on the chemical compositions of clinopyroxenes, Aparicio [30] devised a series of new binary and ternary discrimination diagrams to distinguish the tectonic environments in which their host rocks formed. All these discrimination diagrams distinguish between within-plate volcanism and subduction zone volcanism. As shown in Figure 11, all the analyzed data from Well CK-2 lie within the OIB field, suggesting that these basaltic rocks were formed in an

intraplate tectonic setting, which is consistent with the results determined by the application of the Nisbet and Pearce discrimination diagrams [27].

$$F1 = 0.012 \times \text{SiO}_2 - 0.0807 \times \text{TiO}_2 + 0.0026 \times \text{Al}_2\text{O}_3 - 0.0012 \times \text{FeO}^* - 0.0026 \times \text{MnO} + 0.0087 \times \text{MgO} - 0.0128 \times \text{CaO} - 0.0419 \times \text{Na}_2\text{O};$$

$$F2 = -0.0469 \times \text{SiO}_2 - 0.0818 \times \text{TiO}_2 - 0.0212 \times \text{Al}_2\text{O}_3 - 0.0041 \times \text{FeO}^* - 0.1435 \times \text{MnO} - 0.0029 \times \text{MgO} + 0.0085 \times \text{CaO} + 0.016 \times \text{Na}_2\text{O}$$

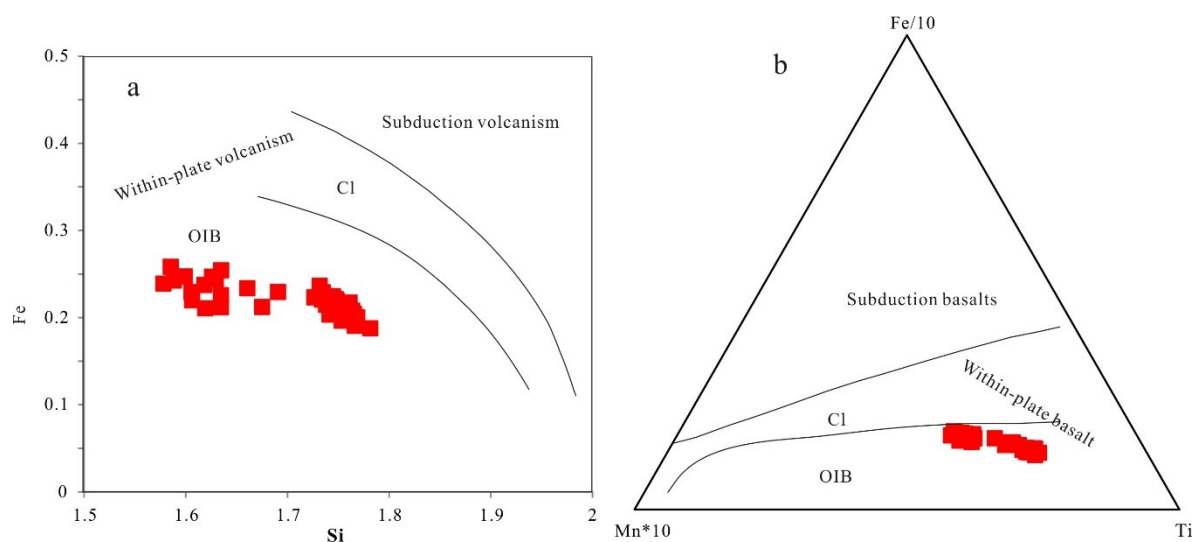


Figure 11. Tectonic discrimination diagrams, proposed by Aparicio [30]. (a) Fe vs. Si tectonic discrimination diagrams; (b) Fe/10-Ti-Mn \times 10 tectonic discrimination diagram for clinopyroxene. CI: alkaline volcanism thinned continental crust, OIB oceanic island basalt.

In general, all the tectonic discrimination diagrams based on clinopyroxene chemistry consistently point out a within-plate alkaline affinity for the parental magma. It seems that the basaltic rocks from Well CK-2 could be considered to have formed in an intraplate tectonic setting environment. Recently, more and more geophysical and geochemical evidence indicates the existence of the mantle plume [9,10,13,14,82–86]. A virtually vertical low velocity cylinder extends beneath the Hainan Island and the SCS, from shallow depths to the 1900 km discontinuity [82]. In addition, the petrological and geochemical data on the SCS and its surrounding areas also suggested the existence of the Hainan mantle plume [3,4,7,9,10,13,14,16,87]. Combined with the regional tectonic evolution, we speculate that these basaltic rocks may be the products of the evolution of a mantle plume. Of course, more geochemical and geological evidence is needed to support this hypothesis.

6. Conclusions

The basement of Well CK-2 consists of basaltic pyroclastic rocks. The phenocryst minerals are mainly clinopyroxene. The clinopyroxenes belong to diopside and fassaite. The mineral chemistry features of the clinopyroxenes show that the parental magma should have belonged to a silica-undersaturated alkaline series, characterized by a high temperature, low pressure, low Si content, high Ca content and low oxygen fugacity. The Al^{IV} content in clinopyroxene mainly depends on the content of SiO_2 in the magma. The electric charge imbalance caused by the replacement of Si by Al is mainly compensated by octahedral Fe^{3+} , followed by minor Ti^{4+} and Al^{3+} . The basaltic pyroclastic rocks may have formed in an intraplate tectonic setting environment.

Supplementary Materials: The following are available online at <http://www.mdpi.com/2075-163X/8/12/575/s1>, Table S1: The LA-ICP-MS analyses of the clinopyroxenes in sample 170 h. Each sample name represents an

individual crystal. Table S2: The LA-ICP-MS analyses of the clinopyroxenes in sample zr1h. Each sample name represents an individual crystal. Table S3: Major element compositions of clinopyroxenes from the basaltic pyroclastic rocks. Calculations are based on 6 oxygens. The data were processed with the geochemical software tool, “Geokit”. Each sample name represents an individual crystal. Table S4: Trace element and REE compositions of the clinopyroxenes from the basaltic pyroclastic rocks. Each sample name represents an individual crystal. Table S5: The calculated melt of the basaltic pyroclastic rocks from Well CK-2.

Author Contributions: Y.Z., K.Y. and H.Q. conceived and designed the experiments; Y.Z. performed the experiments; Y.Z. and H.Q. analyzed the data; and Y.Z. and K.Y. contributed to the writing and revising of the paper.

Funding: This research was funded by the National Science Foundation of China (No. 91428203), the Guangxi scientific projects (Nos. AD17129063 and AA17204074), the Bagui Fellowship from Guangxi Province of China, the PhD research start-up foundation of Guangxi University (XBZ170339), and the basic ability improvement project for young-middle teachers (2018KY0045).

Acknowledgments: We are grateful to two anonymous reviewers who provided constructive suggestions that led to improvement of the paper. We are grateful to Yanwen Tang and Zhihui Dai for LA-ICP-MS analyses.

Conflicts of Interest: The authors declare no conflict of interest.

References

1. Yan, P.; Deng, H.; Liu, H.L.; Zhang, Z.Y.; Jiang, Y.K. The temporal and spatial distribution of volcanism in the South China Sea region. *J. Asian Earth Sci.* **2006**, *27*, 647–659. [[CrossRef](#)]
2. Yan, J.Y.; Li, X.P.; Yan, Q.S. Geochemical characteristics and geological implications of clinopyroxenes in Cenozoic basalts from the South China Sea. *Geol. Rev.* **2014**, *60*, 824–838. (In Chinese with English Abstract)
3. Zhou, H.M.; Xiao, L.; Dong, Y.X.; Wang, C.Z.; Wang, F.Z.; Ni, P.Z. Geochemical and geochronological study of the Sanshui basin bimodal volcanic rock suite, China: Implications for basin dynamics in southeastern China. *J. Asian Earth Sci.* **2009**, *34*, 178–189. [[CrossRef](#)]
4. Xu, Y.G.; Wei, J.X.; Qiu, H.N.; Zhang, H.H.; Huang, X.L. Opening and evolution of the South China Sea constrained by studies on volcanic rocks: Preliminary results and a research design. *Sci. Bull.* **2012**, *57*, 3150–3164. [[CrossRef](#)]
5. Hui, G.G.; Li, S.Z.; Li, X.Y.; Guo, L.L.; Suo, Y.H.; Somerville, I.D.; Zhao, S.J.; Hu, M.Y.; Lan, H.Y.; Zhang, J. Temporal and spatial distribution of Cenozoic igneous rocks in the South China Sea and its adjacent regions: Implications for tectono-magmatic evolution. *Geol. J.* **2016**, *51*, 429–447. [[CrossRef](#)]
6. Song, X.; Li, C.F.; Yao, Y.; Shi, H.S. Magmatism in the evolution of the South China Sea: Geophysical characterization. *Mar. Geol.* **2017**, *394*, 4–15. [[CrossRef](#)]
7. Yan, Q.S.; Shi, X.F.; Wang, K.S.; Bu, W.R.; Xiao, L. Major element, trace element, and Sr, Nd and Pb iso-tope studies of Cenozoic basalts from the South China Sea. *Sci. China Ser. D-Earth* **2008**, *51*, 550–566. [[CrossRef](#)]
8. Yang, S.Y.; Fang, N.Q. Geochemical variation of volcanic rocks from the South China Sea and neighboring land: Implication for magmatic process and mantle structure. *Acta Oceanol. Sin.* **2015**, *34*, 112–124. [[CrossRef](#)]
9. Yan, Q.S.; Shi, X.F.; Metcalfe, I.; Liu, S.F.; Xu, T.Y.; Kornkanitnan, N.; Sirichaiseth, T.; Yuan, L.; Zhang, Y.; Zhang, H. Hainan mantle plume produced late Cenozoic basaltic rocks in Thailand, Southeast Asia. *Sci. Rep.* **2018**, *8*, 2640. [[CrossRef](#)]
10. Yan, Q.S.; Straub, S.; Shi, X.F. Hafnium isotopic constraints on the origin of late Miocene to Pliocene seamount basalts from the South China Sea and its tectonic implications. *J. Asian Earth Sci.* **2018**. [[CrossRef](#)]
11. Zou, H.; Fan, Q. U-Th isotopes in Hainan basalts: Implications for subasthenospheric origin of EM2 mantle end-member and the dynamics of melting beneath Hainan Island. *Lithos* **2010**, *116*, 145–152. [[CrossRef](#)]
12. Li, X.H.; Li, J.B.; Yu, X.; Wang, C.S.; Jourdan, F. $^{40}\text{Ar}/^{39}\text{Ar}$ ages of seamount trachytes from the South China Sea and implications for the evolution of the northwestern sub-basin. *Geosci. Front.* **2015**, *6*, 571–577. [[CrossRef](#)]
13. Liu, E.T.; Wang, H.; Uysal, I.T.; Zhao, J.X.; Wang, X.C.; Feng, Y.X.; Pan, S.Q. Paleogene igneous intrusion and its effect on thermal maturity of organic-rich mudstones in the Beibuwan Basin, South China Sea. *Mar. Petrol. Geol.* **2017**, *86*, 733–750. [[CrossRef](#)]
14. An, A.; Choi, S.; Yu, Y.; Lee, D. Petrogenesis of Late Cenozoic basaltic rocks from southern Vietnam. *Lithos* **2017**, *272–273*, 192–204. [[CrossRef](#)]

15. Zhang, G.L.; Luo, Q.; Zhao, J.; Jackson, M.G.; Guo, L.S.; Zhong, L.F. Geochemical nature of sub-ridge mantle and opening dynamics of the South China Sea. *Earth Planet. Sci. Lett.* **2018**, *489*, 145–155. [[CrossRef](#)]
16. Yan, Q.S.; Shi, X.F.; Wang, K.S.; Bu, W.R. Mineral chemistry and its genetic significance of clinopyroxene in Cenozoic basalts from the South China Sea. *Acta Petrol. Sin.* **2007**, *23*, 2981–2989. (In Chinese with English Abstract)
17. Yan, J.Y.; Li, X.P.; Zhao, L.Q.; Yan, Q.S. Geochemistry of kaersutites in Cenozoic alkali basalts from the South China Sea. *Geol. Rev.* **2015**, *61*, 1434–1446. (In Chinese with English Abstract)
18. Zhang, Z.C.; Xiao, X.C.; Wang, J.; Luo, Z. Mineral Chemistry of the Pulu Cenozoic volcanic rocks in the west Kunlun mountains and its constraints on the magmatic processes. *Acta Mineral. Sin.* **2005**, *25*, 237–248. (In Chinese with English Abstract)
19. Niu, X.L.; Chen, B.; Ma, X. Clinopyroxenes from the Fanshan pluton, Hebei. *Acta Petrol. Sin.* **2009**, *25*, 359–373. (In Chinese with English Abstract)
20. Olin, P.H.; Wolff, J.A. Rare earth and high field strength element partitioning between iron-rich clinopyroxenes and felsic liquids. *Contrib. Mineral. Petrol.* **2010**, *160*, 761–775. [[CrossRef](#)]
21. Guezal, J.; Baghdadi, M.E.; Barakat, A. The Jurassic–Cretaceous volcanism of the Atlas of Beni-Mellal (Central High Atlas, Morocco): Evidence from clinopyroxene composition. *Arab. J. Geosci.* **2015**, *8*, 977–986. [[CrossRef](#)]
22. Wang, K.M.; Wang, Z.Q.; Zhang, Y.L.; Wang, G. Mineral chemistry characteristics and indication significance of clinopyroxene in mafic rock of Gaoqiao area, North Daba Mountains. *Acta Petrol. Mineral.* **2014**, *33*, 527–539. (In Chinese with English Abstract)
23. Liao, R.Q.; Huang, P.; Hu, N.J. A complex magmatic system beneath the middle and northern Okinawa Trough: Evidence from pyroxene characteristics. *Geol. J.* **2017**, *52*, 1059–1068. [[CrossRef](#)]
24. Shu, S.Y.; Yang, X.Y.; Liu, L.; Liu, W.; Cao, J.Y.; Gao, E.G. Dual Geochemical Characteristics for the Basic Intrusions in the Yangtze Block, South China: New Evidence for the Breakup of Rodinia. *Minerals* **2018**, *8*, 288. [[CrossRef](#)]
25. Kushiro, I. Si-Al relation in clinopyroxenes from igneous rock. *Am. J. Sci.* **1960**, *258*, 548–554. [[CrossRef](#)]
26. Verhoogen, J. Distribution of titanium between silicates and oxides in igneous rocks. *Am. J. Sci.* **1962**, *260*, 211–220. [[CrossRef](#)]
27. Nisbet, E.G.; Pearce, J.A. Clinopyroxene composition in mafic lavas from different tectonic settings. *Contrib. Mineral. Petrol.* **1977**, *63*, 149–160. [[CrossRef](#)]
28. Leterrier, J.; Maury, R.C.; Thonon, P.; Girard, D.; Marchal, M. Clinopyroxene composition as a method of identification of the magmatic affinities of paleovolcanic series. *Earth Planet. Sci. Lett.* **1982**, *59*, 139–154. [[CrossRef](#)]
29. Seyler, M.; Bonatti, E. Na, Al^{IV}, and Al^{VI}, in clinopyroxenes of subcontinental and suboceanic ridge peridotites: A clue to different melting processes in the mantle? *Earth Planet. Sci. Lett.* **1994**, *122*, 281–289. [[CrossRef](#)]
30. Aparicio, A. Relationship between clinopyroxene composition and the formation environment of volcanic host rocks. *IUP J. Earth Sci.* **2010**, *4*, 1–11.
31. Niu, X.L.; Yang, J.S.; Fei, L.; Zhang, H.Y.; Yang, M.C. Origin of Baotoudong syenites in North China Craton: Petrological, mineralogical and geochemical evidence. *Sci. China Earth Sci.* **2016**, *59*, 95–110. [[CrossRef](#)]
32. Kargin, A.V.; Sazonova, L.V.; Nosova, A.A.; Tretyachenko, V.V. Composition of garnet and clinopyroxene in peridotite xenoliths from the Grib kimberlite pipe, Arkhangelsk diamond province, Russia: Evidence for mantle metasomatism associated with kimberlite melts. *Lithos* **2016**, *262*, 442–455. [[CrossRef](#)]
33. Kil, Y.; Shin, H.S.; Oh, H.Y.; Kim, J.S.; Choi, M.S.; Shin, H.J.; Park, C.S. In-situ trace element analysis of clinopyroxene on thin section by using LA-ICP-MS. *Geosci. J.* **2011**, *15*, 177–183. [[CrossRef](#)]
34. Hart, S.R.; Dunn, T. Experimental cpx/melt partitioning of 24 trace elements. *Contrib. Mineral. Petrol.* **1993**, *113*, 1–8. [[CrossRef](#)]
35. Gilman, T.; Feineman, M.; Fisher, D. The Chulitna terrane of south-central Alaska: A rifted volcanic arc caught between the Wrangellia composite terrane and the Mesozoic margin of North America. *Geol. Soc. Am. Bull.* **2009**, *121*, 979–991. [[CrossRef](#)]
36. Huang, X.L.; Niu, Y.; Xu, Y.G.; Chen, L.L.; Yang, Q.J. Mineralogical and Geochemical Constraints on the Petrogenesis of Post-collisional Potassic and Ultrapotassic Rocks from Western Yunnan, SW China. *J. Petrol.* **2010**, *51*, 1617–1654. [[CrossRef](#)]

37. Sun, J.; Liu, C.Z.; Wu, F.Y.; Yang, Y.H.; Chu, Z.Y. Metasomatic origin of clinopyroxene in Archean mantle xenoliths from Hebi, North China Craton: Trace-element and Sr-isotope constraints. *Chem. Geol.* **2012**, *328*, 123–136. [[CrossRef](#)]
38. Rollinson, H.; Gravestock, G. The trace element geochemistry of clinopyroxenes from pyroxenites in the Lewisian of NW Scotland: Insights into light rare earth element mobility during granulite facies metamorphism. *Contrib. Mineral. Petrol.* **2012**, *163*, 319–335. [[CrossRef](#)]
39. Zuo, P.; Liu, X.; Hao, J.; Wang, Y.S.; Zhao, R.; Ge, S.S. Chemical compositions of garnet and clinopyroxene and their genetic significances in Yemaquan skarn iron-copper-zinc deposit, Qimantagh, eastern Kunlun. *J. Geochem. Explor.* **2015**, *158*, 143–154. [[CrossRef](#)]
40. Xue, S.C.; Qin, K.Z.; Tang, D.M.; Mao, Y.J.; Yao, Z.S. Compositional characteristics of pyroxenes from Permian maficultramafic complexes in Eastern Xinjiang, and their implications for petrogenesis and Ni-Cu mineralization. *Acta Petrol. Sin.* **2015**, *31*, 2175–2192. (In Chinese with English Abstract)
41. Jankovics, M.É.; Taracsák, Z.; Dobosi, G.; Embey-Isztin, A.; Batki, A.; Harangi, S.; Hauzenbergere, C.A. Clinopyroxene with diverse origins in alkaline basalts from the western Pannonian Basin: Implications from trace element characteristics. *Lithos* **2016**, *262*, 120–134. [[CrossRef](#)]
42. Batki, A.; Pál-Molnár, E.; Jankovics, M.É.; Kerr, A.C.; Kiss, B.; Markl, G.; Heincz, A.; Harangi, S. Insights into the evolution of an alkaline magmatic system: An in situ trace element study of clinopyroxenes from the Ditrău Alkaline Massif, Romania. *Lithos* **2018**, *300–301*, 51–71. [[CrossRef](#)]
43. Qiu, J.X.; Liao, Q.A. Petrogenesis and cpx mineral chemistry of Cenozoic basalts from Zhejiang and Fujian of eastern China. *Volcanol. Mineral. Resour.* **1996**, *17*, 16–25. (In Chinese with English Abstract)
44. Krátký, O.; Rappich, V.; Racek, M.; Míková, J.; Magna, T. On the Chemical Composition and Possible Origin of Na-Cr-Rich Clinopyroxene in Silico carbonatites from Samalpatti, Tamil Nadu, South India. *Minerals* **2018**, *8*, 355. [[CrossRef](#)]
45. Campbell, I.H.; Borley, G.D. The geochemistry of pyroxenes from the lower layered series of the Jemberlana intrusion, Western Australia. *Contrib. Mineral. Petrol.* **1974**, *47*, 281–297. [[CrossRef](#)]
46. Vuorinen, J.H.; Hålenius, U.; Whitehouse, M.J.; Mansfeld, J.; Skelton, A.D.L. Compositional variations (major and trace elements) of clinopyroxene and Ti-andradite from pyroxenite, ijolite and nepheline syenite, Alnö Island, Sweden. *Lithos* **2005**, *81*, 55–77. [[CrossRef](#)]
47. Yao, B.C.; Wan, L.; Wu, N.Y. Cenozoic plate tectonic activities in the Great South China Sea area. *Geol. China* **2004**, *31*, 113–122. (In Chinese with English Abstract)
48. Yan, Q.S.; Castillo, P.; Shi, X.F.; Wang, L.L.; Liao, L.; Ren, J.B. Geochemistry and petrogenesis of volcanic rocks from Daimao Seamount (South China Sea) and their tectonic implications. *Lithos* **2015**, *218–219*, 117–126. [[CrossRef](#)]
49. Taylor, B.; Hayers, D.E. The tectonic evolution of the South China Sea. In *The Tectonic and Geological Evolution of the Southeast Asian Seas and Islands*, *Geophys. Monogr. Ser.*; Hayers, D.E., Ed.; American Geophysical Union: Washington, DC, USA, 1980; Volume 23, pp. 89–104.
50. Briais, A.; Patriat, P.; Tapponnier, P. Updated interpretation of magnetic anomalies and seafloor spreading stages in the South China Sea: Implications for the Tertiary tectonics of Southeast Asia. *J. Geophys. Res. Solid Earth* **1993**, *98*, 6299–6328. [[CrossRef](#)]
51. Kido, Y.; Suyehiro, K.; Kinoshita, H. Rifting to spreading process along the northern continental margin of the South China Sea. *Mar. Geophys. Res.* **2001**, *22*, 1–15. [[CrossRef](#)]
52. Li, C.F.; Xu, X.; Lin, J.; Sun, Z.; Zhu, J.; Yao, Y.J.; Zhao, X.X.; Liu, Q.S.; Kulhanek, D.K.; Wang, J.; et al. Ages and magnetic structures of the South China Sea constrained by deep tow magnetic surveys and IODP Expedition 349. *Geochem. Geophys. Geosyst.* **2014**, *15*, 4958–4983. [[CrossRef](#)]
53. Li, C.F.; Li, J.B.; Ding, W.W.; Franke, D.; Yao, Y.J.; Shi, H.S.; Pang, X.; Cao, Y.; Lin, J.; Kulhanek, D.K.; et al. Seismic stratigraphy of the central South China Sea basin and implications for neotectonics. *J. Geophys. Res. (Solid Earth)* **2015**, *120*, 1377–1399. [[CrossRef](#)]
54. Xie, A.Y.; Zhong, L.F.; Yan, F. Time and genesis of Cenozoic magmaticcs in the South China Sea and surrounding areas. *Mar. Geol. Quat. Geol.* **2017**, *37*, 108–118. (In Chinese with English Abstract)
55. Yan, Q.S.; Shi, X.F.; Castillo, P. The late Mesozoic-Cenozoic tectonic evolution of the South China Sea: A petrologic perspective. *J. Asian Earth Sci.* **2014**, *85*, 178–201. [[CrossRef](#)]

56. Wang, R.; Yu, K.F.; Jones, B.; Wang, Y.H.; Zhao, J.X.; Feng, Y.X.; Bian, L.Z.; Xu, S.D.; Fan, T.L.; Jiang, W.; et al. Evolution and development of Miocene “island dolostones” on Xisha Islands, South China Sea. *Mar. Geol.* **2018**, *406*, 142–158. [[CrossRef](#)]
57. Zhang, Y.; Yu, K.Y.; Qian, H.D.; Fan, T.L.; Yue, Y.F.; Wang, R.; Jang, W.; Xu, S.D.; Wang, Y.H. The basement and volcanic activities of the Xisha Islands: Evidence from the kilometer-scale drilling in the northwestern South China Sea. *Geol. J.* **2019**, in press.
58. Liu, Y.S.; Hu, Z.C.; Gao, S.; Günther, D.; Xu, J.; Gao, C.G.; Chen, H.H. In situ analysis of major and trace elements of anhydrous minerals by LA-ICP-MS without applying an internal standard. *Chem. Geol.* **2008**, *257*, 34–43. [[CrossRef](#)]
59. GeoReM Database. Available online: <http://georem.mpch-mainz.gwdg.de/> (accessed on 6 December 2019).
60. Liu, Y.S.; Gao, S.; Hu, Z.C.; Gao, C.G.; Zong, K.Q.; Wang, D.B. Continental and oceanic crust recycling-induced melt-peridotite interactions in the Trans-North China Orogen: U-Pb dating, Hf isotopes and trace elements in zircons of mantle xenoliths. *J. Petrol.* **2010**, *51*, 537–571. [[CrossRef](#)]
61. Lu, Y.F. Geolit—A geochemical toolkit for Microsoft Excel. *Geochimica* **2004**, *33*, 459–464. (In Chinese with English Abstract)
62. Wass, S.Y. Multiple origins of clinopyroxenes in alkali basaltic rocks. *Lithos* **1979**, *12*, 115–132. [[CrossRef](#)]
63. Morimoto, N. Nomenclature of Pyroxenes. *Mineral. Petrol.* **1988**, *39*, 55–76. [[CrossRef](#)]
64. Hauri, E.H.; Hart, S.R. Constraints on melt migration from mantle plumes: A trace element study of peridotite xenoliths from Savai'i, Western Samoa. *J. Geophys. Res. Solid Earth* **1994**, *99*, 24301–24321. [[CrossRef](#)]
65. Liu, Y.R.; Lv, X.B.; Mei, W.; Dai, Y.C. Mineralogy of clinopyroxene from Pobei mafic-ultramafic complex in Beishan area, Xinjiang, and its geological significance. *Acta Petrol. Mineral.* **2012**, *31*, 212–224. (In Chinese with English Abstract)
66. LeBas, M.J. The rock of aluminium in igneous clinopyroxenes with relation to their parentage. *Am. J. Sci.* **1962**, *260*, 267–288. [[CrossRef](#)]
67. Tang, D.M.; Qin, K.Z.; Chen, B.; Ma, Y.J.; Guo, H.; Evans, N.J. Mineral chemistry and genesis of the Permian Cihai and Cinan magnetite deposits, Beishan, NW China. *Ore Geol. Rev.* **2017**, *86*, 79–99. [[CrossRef](#)]
68. Aoki, K.; Shiba, I. Clinopyroxenes from alkaline rocks of Japan. *Am. Mineral.* **1964**, *49*, 1199–1223.
69. Lai, S.C.; Qin, J.F.; Li, Y.F. Trace element geochemistry and classification of the clinopyroxene in Cenozoic trachybasalt from north Qiangtang area, Tibetan Plateau. *J. Northwest Univ. (Nat. Sci. Ed.)* **2005**, *25*, 611–616.
70. Gibb, F.G.F. The Zoned Clinopyroxenes of the Shiant Isles Sill, Scotland. *J. Petrol.* **1973**, *14*, 203–230. [[CrossRef](#)]
71. Sherafat, S.; Yavuz, Y.; Noorbehesht, I.; Yildirim, D.K. Mineral chemistry of Plio-Quaternary subvolcanic rocks, southwest Yazd Province, Iran. *Int. Geol. Rev.* **2012**, *54*, 1497–1531. [[CrossRef](#)]
72. Bondi, M.; Morten, L.; Nimis, P.L.; Tranne, C.A. Megacrysts and mafic-ultramafic xenolith-bearing ignimbrites from Sirwa Volcano, Morocco: Phase petrology and thermobarometry. *Mineral. Petrol.* **2002**, *75*, 203–221. [[CrossRef](#)]
73. Thompson, R.N. Some High-Pressure Pyroxenes. *Mineral. Mag.* **1974**, *39*, 768–787. [[CrossRef](#)]
74. Neumann, E.R.; Marti, J.; Mitjavila, J.; Wulff-Pedersen, E. Origin and implications of marie xenoliths associated with Cenozoic extension-related volcanism in the Valencia Trough, NE Spain. *Mineral. Petrol.* **1999**, *65*, 113–139. [[CrossRef](#)]
75. Niu, X.L.; Chen, B.; Liu, A.K.; Suzuki, K.; Ma, X. Petrological and Sr-Nd-Os isotopic constraints on the origin of the Fanshan ultrapotassic complex from the North China Craton. *Lithos* **2012**, *149*, 146–158. [[CrossRef](#)]
76. Wandji, P.; Tsafack, J.P.F.; Bardintzeff, J.M.; Nkouathio, D.G.; Dongmo, A.K.; Bellon, H.; Guillou, H. Xenoliths of dunites, wehrlites and clinopyroxenites in the basanites from Batoke volcanic cone (Mount Cameroon, Central Africa): Petrogenetic implications. *Mineral. Petrol.* **2009**, *96*, 81–98. [[CrossRef](#)]
77. Zou, J.X.; Liu, X.F.; Deng, J.H.; Dong, Y.; Dong, Y.P. Compositional characteristics of clinopyroxenes from the Luoji ophiolitic mélange in Shangri-La County, Yunnan Province. *Geol. China* **2013**, *40*, 1806–1817.
78. Zou, J.X.; Liu, X.F.; Deng, J.H.; Li, C.H.; Huang, Y.P.; Dong, Y.; Yi, L.W. Mineralogical composition characteristics and geological significance of the clinopyroxene from ultrabasic-basic rocks at Luoji Village, Shangri-La County, Yunnan Province. *Acta Petrol. Mineral.* **2012**, *31*, 701–711.
79. Wang, X.C.; Li, Z.X.; Li, X.H.; Li, J.; Liu, Y.; Long, W.G.; Zhou, J.B.; Wang, F. Temperature, pressure, and composition of the mantle source region of Late Cenozoic basalts in Hainan Island, SE Asia: A consequence of a young thermal mantle plume close to subduction zones? *J. Petrol.* **2012**, *53*, 177–233. [[CrossRef](#)]

80. Wang, X.C.; Li, Z.X.; Li, X.H.; Li, J.; Xu, Y.G.; Li, X.H. Identification of an ancient mantle reservoir and young recycled materials in the source region of a young mantle plume: Implications for potential linkages between plume and plate tectonics. *Earth Planet. Sci. Lett.* **2013**, *377*, 248–259. [[CrossRef](#)]
81. Sun, S.S.; McDonough, W.F. Chemical and isotopic systematic of oceanic basalts: Implications for mantle composition and processes. In *Magmatism in Ocean Basins*; Saunders, A.D., Norry, M.J., Eds.; Geological Society London Special Publications: London, UK, 1989; pp. 313–345.
82. Lebedev, S.; Nolet, G. Upper mantle beneath Southeast Asia from S velocity tomography. *J. Geophys. Res.* **2003**, *108*, 20–48. [[CrossRef](#)]
83. Montelli, R.; Nolet, G.; Dahlen, F.A.; Masters, M.; Engdahl, E.B.; Hung, S.H. Finite-frequency tomography reveals a variety of plumes in the mantle. *Sci. Bull.* **2004**, *303*, 338–343. [[CrossRef](#)]
84. Zhao, D.P. Seismic images under 60 hotspots: Search for mantle plumes. *Gondwana Res.* **2007**, *12*, 335–355. [[CrossRef](#)]
85. Yan, Q.S.; Shi, X.F. Hainan Mantle Plume and the Formation and Evolution of the South China Sea. *Geol. J. China Univ.* **2007**, *13*, 311–322.
86. Lei, J.S.; Zhao, D.P. New seismic constraints on the upper mantle structure of the Hainan plume. *Phys. Earth Planet. Inter.* **2009**, *173*, 33–50. [[CrossRef](#)]
87. Li, N.S.; Yan, Q.S.; Chen, Z.H.; Shi, X.F. Geochemistry and petrogenesis of Quaternary volcanism from the islets in the eastern Beibu Gulf: Evidence for Hainan plume. *Acta Oceanol. Sin.* **2013**, *32*, 40–49. [[CrossRef](#)]



© 2018 by the authors. Licensee MDPI, Basel, Switzerland. This article is an open access article distributed under the terms and conditions of the Creative Commons Attribution (CC BY) license (<http://creativecommons.org/licenses/by/4.0/>).